

## Three-dimensional Momentum and Heat Transport in a Turbulent Cylinder Wake

H.L.Cao<sup>1</sup>, J.G.Chen<sup>1</sup>, T. Zhou<sup>2</sup>, R.A.Antonia<sup>3</sup> and Y.Zhou<sup>1</sup>

<sup>1</sup> Institute for Turbulence-Noise-Vibration Interaction and Control, Shenzhen Graduate School, Harbin Institute of Technology, Shenzhen 518055, China

<sup>2</sup> School of Civil and Resource Engineering, The University of Western Australia,  
 35 Stirling Highway, Crawley, WA 6009, Australia

<sup>3</sup> School of Engineering, University of Newcastle, NSW 2308, Australia

### Abstract

This work aims to provide insight into the three-dimensional aspects of momentum and heat transport in a turbulent cylinder wake. All three components of the velocity and vorticity vectors, along with the fluctuating temperatures, were simultaneously measured with an 8 hot-wire vorticity probe and four cold-wire probes. A phase-averaging technique has been developed to detect reliably the coherent events, thus allowing the coherent contributions from various quantities associated with the vector as well as passive scalar fields to be quantified accurately. While the coherent heat flux is largely associated with spanwise vortex rolls, the incoherent (or ‘remainder’) heat flux occurs between two successive opposite-signed vortices, rather than in the saddle region, as one might have expected. A 3-D conceptual model is suggested, which is consistent with a previous 2-D model in the plane of mean shear, to account more accurately for the role played by the rib structures in transporting heat and momentum.

### Introduction

The flow around a circular cylinder is of intrinsic interest and has received significant attention by researchers from the point of view of coherent structures (Hussain 1983). The mechanism for mass transfer is similar to that of heat transfer, when mass and heat are treated as passive scalars. It is therefore important to understand the transport characteristics of passive scalars in the turbulent wake. The previous investigation has uncovered the topology of the velocity and temperature field, as well as the coherent structures in the turbulent near wake (Matsumura & Antonia 1993; Yiu et al. 2004a; Zhou & Yiu 2006). Matsumura & Antonia (1993) investigated momentum and passive heat transport characteristics in a single cylinder wake at a Reynolds number of 5830, and gave a simplified two-dimensional sketch of flow topology. Zhou & Yiu (2006) studied the passive scalar transport in the wake of two tandem cylinders, with a centre-to-centre spacing ratio  $L/d$  varying from 1.3 to 6.0. They found that coherent and incoherent heat flux vectors show significant variation for different  $L/d$ . The three-dimensional vortex structure in the turbulent wake has been captured by flow visualizations (Wu et al. 1996; Huang et al. 2006; Scarano & Poelma 2009), which may lead to three-dimensional heat transport behaviour. However, the simultaneous measurement of all three vorticity components and the fluctuating temperature has proven to be a challenge. Experimental efforts to obtain all three components of the vorticity vector are reported by Marasli et al. (1993), Mi & Antonia (1996), Zhang et al (2000) and Yiu et al. (2004b). To provide reliable three-dimensional vorticity data is important for the thorough understanding of heat transport characteristics of the flow.

In this study, the three components of vorticity vectors were measured with the temperature fluctuation simultaneously using

a vorticity probe (consists of four X-wires) and four cold-wire probes. An enhanced phase average method was developed to detect the coherent structure and the remainder part. The main aim of the present study is to examine in detail the contributions from the coherent and incoherent motions to the heat transport.

### Experimental details

The experiments were conducted in a close-loop wind tunnel with a working section of  $1.2\text{m} \times 0.8\text{m}$  and  $2.0\text{m}$  long. The free stream turbulence intensity is less than 0.5%. A circular cylinder with a diameter  $d=12.7\text{mm}$  was used to generate the wake. The free-stream velocity  $U_1$  was  $3\text{m/s}$ , corresponding to a Reynolds number  $Re (= U_1 d / \nu)$  of 2540. The measurement locations were at  $x/d=10, 20$  and  $40$  (where  $x$  is the streamwise distance from the cylinder). However, due to the page limitation, only the results at  $x/d=10$  will be reported here.

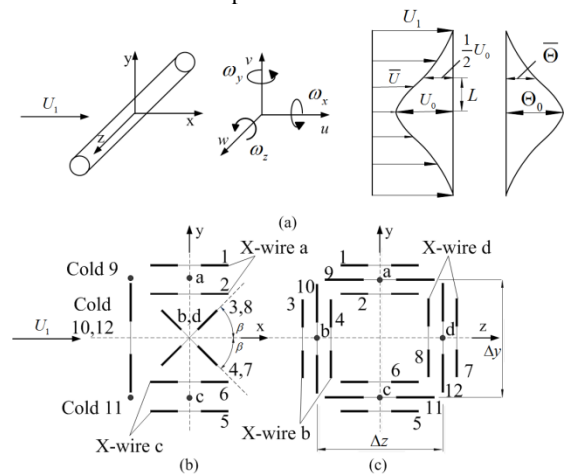


Figure 1. Experimental arrangement and coordinate system and sketches of the vorticity probe: (a) experimental arrangement, coordinate system, and definition sketch; (b) side view of the probe, (c) front view of the probe.

A probe consisting of four X-wires (Figure 1) and four cold wires were used to measure the velocity and temperature fluctuations simultaneously. Two of the X-wires (X-wires b and d) were aligned in the  $x-y$  plane and separated by  $\Delta z = 2.7\text{mm}$  in the  $z$  direction; the other two (X-wires a and c) were in the  $x-z$  plane and separated by  $\Delta y = 2.0\text{mm}$  in the  $y$  direction. The four cold wires were placed about  $1\text{mm}$  upstream of the vorticity probe. The separations  $\Delta y$  and  $\Delta z$  between the opposite cold wires are about  $2.5\text{mm}$  and  $2.2\text{mm}$ . Then  $u, v, w$  and  $\theta$  may be considered to be obtained at normally the same point. The maximum mean

temperature excess  $\Theta_0$  on the centerline of the wake is about 1.6°C, relative to the ambient. This value is small enough to avoid any buoyancy effect, so heat could be considered as a passive scalar.

The hot and cold wires were etched from Wollaston (Pt-10%Rh) wires. The active lengths are about  $200 d_w$  and  $800 d_w$  for the hot and cold wires, respectively (where  $d_w$  is the diameter of the wires and equals to  $2.5 \mu\text{m}$  for the hot wires and  $1.27 \mu\text{m}$  for the cold wires). The hot wires were operated with in-house constant temperature circuits at an overheat ratio of 1.5. The cold wires were operated with constant current (0.1 mA) circuits. The probe was calibrated at the centerline of the tunnel using a Pitot static tube connected to a MKS Baratron pressure transducer. The yaw calibration was performed over  $\pm 20$  deg. The output signals from the anemometers were passed through buck and gain circuits and low-pass filtered at a cutoff frequency  $f_c$  of 1250 Hz. The filtered signals were subsequently sampled at a frequency  $f_s = 2f_c$  using a 16 bit analog-to-digital converter. The duration of data was about 45 s.

## Results and discussion

Since the vorticity components are calculated using the velocity signals from the four X-wires, it is important to ensure that the velocity signals were measured properly. Figure 2 shows the power spectra of the measured velocity signals from the 4 X-wires and temperature signals from the 4 cold wires at  $x/d=10$  and  $y/d=0.39$  (near the vortex centre). The spectra display a pronounced peak at  $St=0.2$ , especially in  $E_v$  (figure 2b). The second harmonic is also discernible in  $E_u$  and  $E_\theta$ . The spectra of  $u$  (or  $v$  and  $w$ ) from different cross-wires show a good overlap, suggesting little interference between the wires.

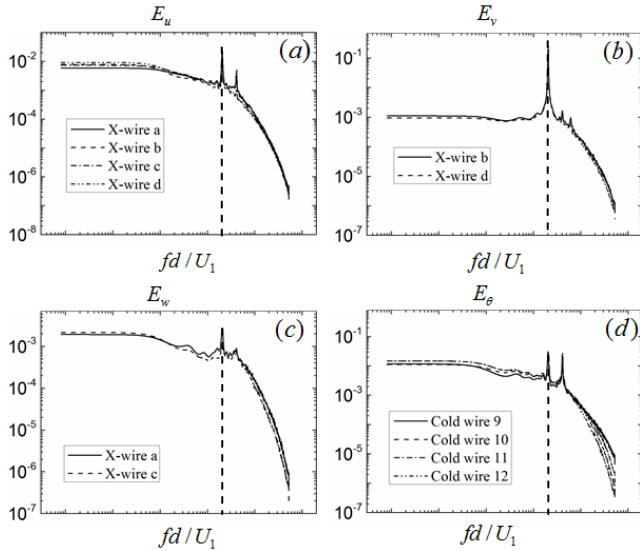


Figure 2. Power spectra of  $u$ ,  $v$ ,  $w$ , and  $\theta$  at  $x/d=10$ . Dashed lines stand for the positions where the Strouhal number  $St=0.2$ .

The coherent vorticity field can be extracted using a phase-averaging method, which is similar to that used by Zhou et al. (2002). A cross correlation between the reference signal  $v$  and filtered signal  $v_f$  was done to avoid any phase shift caused by the filtering process, thus allowing a better detection of the organized structures. The phase average of an instantaneous quantity  $B$  is given by  $\langle B \rangle_k = \frac{1}{N} \sum_{i=1}^N B_{k,i}$ , where  $k$  represents phase.  $N$  is the total number of detections, which is about 1980.  $B$  can be considered as the sum of the time mean component

$\bar{B}$  and the fluctuating component  $\beta$ . The latter can be further decomposed into a coherent fluctuation  $\tilde{\beta} \equiv \langle \beta \rangle$  and a remainder  $\beta_r$ . Also,  $\langle \beta \gamma \rangle = \tilde{\beta} \tilde{\gamma} + \langle \beta_r \gamma_r \rangle$ , where  $\beta$  and  $\gamma$  represents for either  $u, v, w$  or  $\theta$ .

Figure 3 presents the iso-contours of three coherent vorticity components  $\tilde{\omega}_x^*$ ,  $\tilde{\omega}_y^*$  and  $\tilde{\omega}_z^*$ . The phase  $\phi$ , ranging from  $-2\pi$  to  $+2\pi$ , can be interpreted in terms of a longitudinal distance. The positions of centres and saddle points, estimated from sectional streamlines (not shown), are denoted by + and x, respectively. An asterisk indicates hereinafter normalization by  $U_1$ ,  $d$  and the maximum mean temperature excess  $\Theta_0$  in the wake. The  $\tilde{\omega}_x^*$ ,  $\tilde{\omega}_y^*$  contours are identifiable and the maximum is about twice of that reported by Zhou et al (2003), which may be attributed to the improved detection technique. And there is a resemblance between  $\tilde{\omega}_z^*$  and  $\tilde{\omega}_x^*$  at  $x/d=10$ , suggesting the combined effect of the three-dimensionality of spanwise structures and rib-like structures.

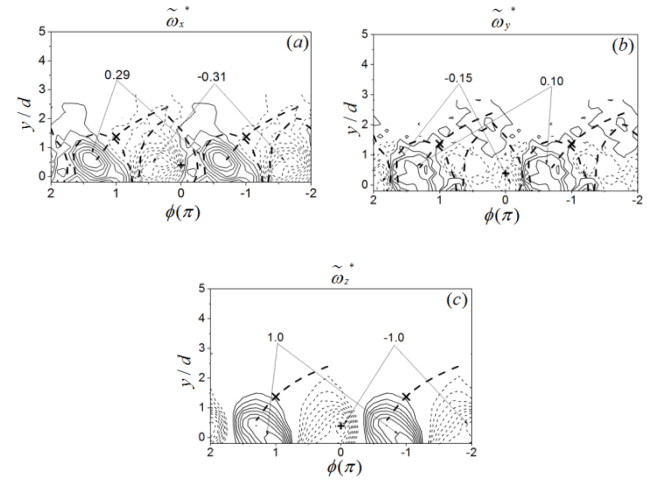


Figure 3. Phase-averaged vorticity contours  $\tilde{\omega}^*$ . Contour interval (a-c): 0.042, 0.031, 0.102; The thicker dashed line denotes the outermost vorticity contours of  $\tilde{\omega}_z^*$ , and the diverging separatrix.

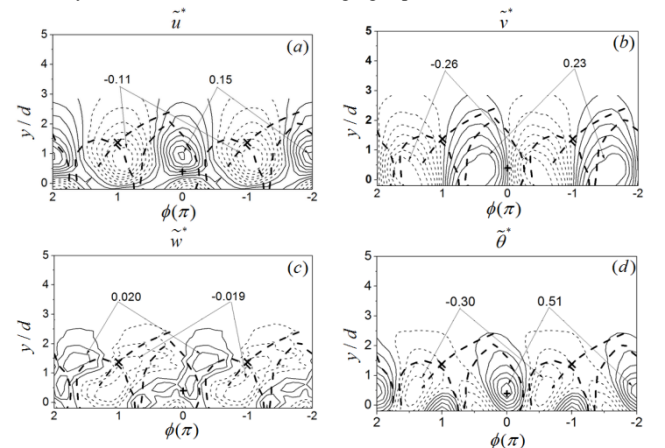


Figure 4. Phase-averaged velocity and temperature fluctuations. Contour interval: (a-d): 0.020, 0.041, 0.0066, 0.089.

The phase-averaged velocity and temperature fluctuations  $\tilde{u}^*$ ,  $\tilde{v}^*$ ,  $\tilde{w}^*$  and  $\tilde{\theta}^*$  at  $x/d=10$  are given in Figure 4. The appearance and magnitude of the  $\tilde{u}^*$  and  $\tilde{v}^*$  contours are similar to that reported previously (Zhou et al. 2002) and will not be discussed further. Notice that the maximum magnitude of  $\tilde{w}^*$  is one order

of magnitude smaller than that of  $\tilde{v}^*$ . And the negative  $\tilde{w}^*$  contour is stretched along the diverging separatrix. The positive and negative contours of  $\tilde{w}^*$  are separated by the divergent separatrix, suggesting the induction effect of the rib-like structures which should be aligned with the diverging separatrix. The  $\tilde{\theta}^*$  contours centred on the vortex at  $\phi = 0$  are flanked by negative contours which result from the strong engulfment of upstream ambient fluid. Figure 5 presents the phase-averaged coherent Reynolds shear stress  $\tilde{u}^* \tilde{v}^*$ , heat fluxes  $\tilde{u}^* \tilde{\theta}^*$ ,  $\tilde{v}^* \tilde{\theta}^*$  and  $\tilde{w}^* \tilde{\theta}^*$  at  $x/d=10$ . The patterns and magnitude of  $\tilde{u}^* \tilde{v}^*$ ,  $\tilde{u}^* \tilde{\theta}^*$  and  $\tilde{v}^* \tilde{\theta}^*$  are similar to those reported by Zhou et al.(2002). The positive  $\tilde{u}^* \tilde{\theta}^*$  contours (figure 5b) are dominant and the  $\tilde{v}^* \tilde{\theta}^*$  contours (figure 5c) are anti-symmetrical about the vortex centre, due to the association of both positive and negative  $\tilde{v}$  with the warm fluid within the spanwise vortices. It can be also seen that the maximum positive  $\tilde{w}^* \tilde{\theta}^*$  (figure 5d) is close to the vortex centre and is stretched through the saddle point along the diverging separatrix. This suggests that the spanwise heat flux component is influenced both by the spanwise rolls and the rib-like streamwise vortices.

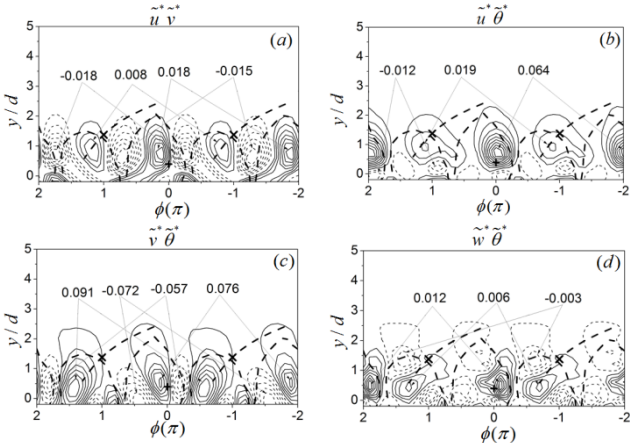


Figure 5. Phase averaged coherent momentum flux and heat flux. Contour interval: (a-d):0.0026, 0.0076, 0.015, 0.0015.

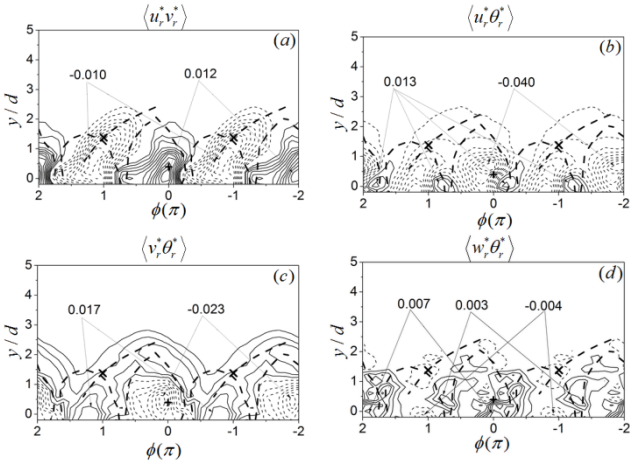


Figure 6. Phase-averaged incoherent momentum flux and heat fluxes. Contour interval: (a-d): 0.001, 0.0048, 0.0037, 0.0014.

Figure 6 contains the incoherent Reynolds shear stress and heat fluxes. It is expected that the  $\langle u_r^* v_r^* \rangle$  contours (figure 6a) are stretched in the direction of the diverging separatrix whilst the

negative extremum of  $\langle u_r^* v_r^* \rangle$  is near the saddle point. On the other hand, the positive extremum of  $\langle u_r^* v_r^* \rangle$  occurs near the vortex centre and gradually moves towards the centerline. The  $\langle u_r^* v_r^* \rangle$  contours are quite comparable to their coherent counterparts (figure 5a). However, the maximum magnitude of the positive  $\langle u_r^* \theta_r^* \rangle$  (figure 6b) or  $\langle v_r^* \theta_r^* \rangle$  (figure 6c) contours is smaller than that of their coherent counterparts. In addition, the positive  $\langle v_r^* \theta_r^* \rangle$  wrap around two consecutive vortices. It seems that the positive  $\langle w_r^* \theta_r^* \rangle$  contours (figure 6d) appear in the alley between neighbouring vortices whilst the negative  $\langle w_r^* \theta_r^* \rangle$  contours occur near the saddle points.

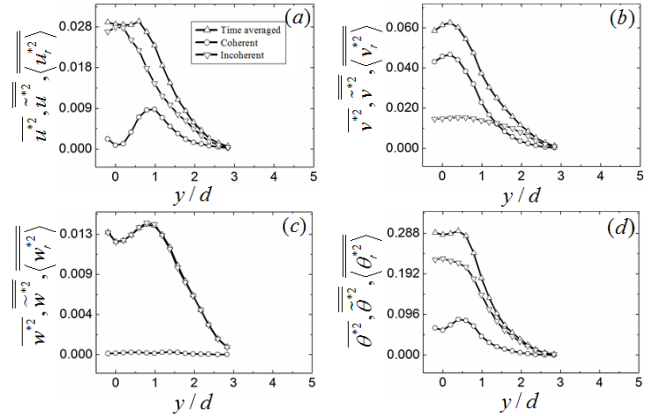


Figure 7. Coherent and incoherent contributions to time-averaged Reynolds stresses and temperature variance.

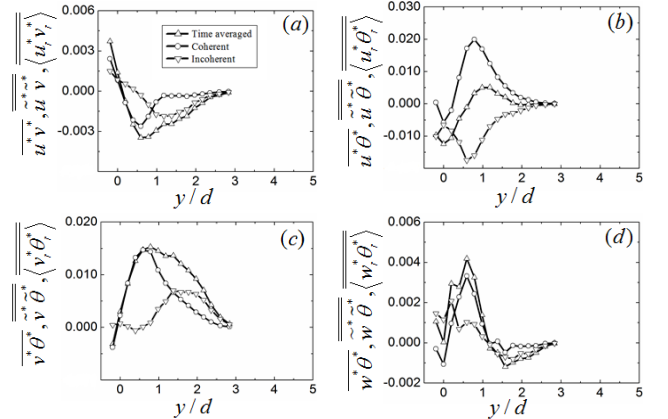


Figure 8. Coherent and incoherent contributions to time-averaged Reynolds shear stress and heat fluxes.

We next quantify the contributions to conventional Reynolds stresses and heat fluxes from the coherent structures and the “remaining” motion. Figures 7 and 8 include coherent and incoherent contributions to time-averaged Reynolds stresses, temperature variance and heat fluxes. The coherent motion makes a more important contribution to  $\overline{v^2}$  than to  $\overline{u^2}$  or  $\overline{\theta^2}$ , with negligible contribution to  $\overline{w^2}$ . The coherent contribution to  $\overline{uv}$  and  $\overline{v\theta}$  (figure 8) is considerably larger than that to  $\overline{u\theta}$ , as observed by Matsumura & Antonia (1993). The coherent contribution accounts almost entirely for  $\overline{uv}$  and  $\overline{v\theta}$  for  $y^* < 0.5$ . For  $y^* > 1.0$ , this contribution is due mainly to the incoherent motion. The coherent contributions to  $\overline{v\theta}$  and

$w\theta$  are quite similar, even though the magnitude of the latter is much smaller.

The characteristics of heat transport can be examined by means of the coherent heat flux vector  $\tilde{q}^*$  ( $\equiv (\tilde{u}\tilde{\theta}, \tilde{v}\tilde{\theta}, \tilde{w}\tilde{\theta})$ , figure 9b) and incoherent heat flux vector  $\tilde{q}_r^*$  ( $\equiv (\langle u_r^*\theta_r^* \rangle, \langle v_r^*\theta_r^* \rangle, \langle w_r^*\theta_r^* \rangle)$ ,

figure 9c) along with the coherent velocity vector  $\tilde{V}^*$  (figure 9a). It shows that a small amount of the coherent heat flux vector  $\tilde{q}^*$  is aligned with the velocity vectors near the vortex centres, and most of  $\tilde{q}^*$  point upwards. It clearly shows that the coherent motion within the core region near the vortex centre contributes little to the transport of heat out of vortex rolls, while the coherent motion near the vortex border contributes in a major way to the heat transport. The incoherent heat flux vectors  $\tilde{q}_r^*$  generally cross the vortex border and point towards the diverging separatrix. They are quite different from  $\tilde{q}^*$ , suggesting that the incoherent motions not only contribute to heat transport out of the vortices, but are also responsible for the heat transport between consecutive spanwise vortices of the same sign.

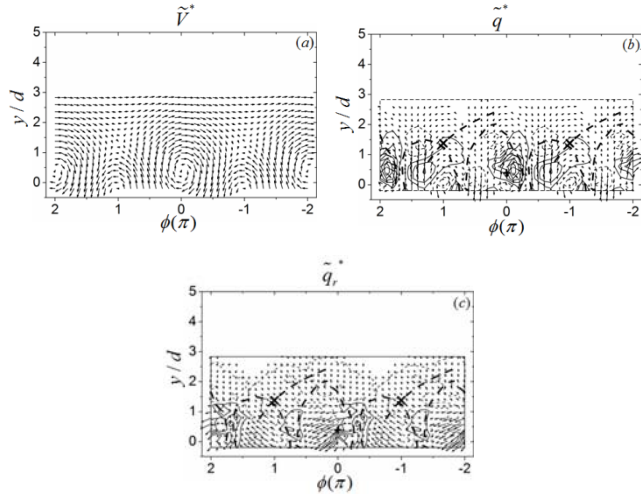


Figure 9. Phase-averaged coherent velocity vectors  $\tilde{V}^*$  (a) in a reference frame moving at  $U_c$ ; (b) Coherent heat flux vector  $\tilde{q}^*$ : vectors are used for  $(\tilde{u}\tilde{\theta}, \tilde{v}\tilde{\theta})$  and iso-contours are used for  $\tilde{w}\tilde{\theta}$ ; (c) Incoherent heat flux vector  $\tilde{q}_r^*$ : vectors are used for  $(\langle u_r^*\theta_r^* \rangle, \langle v_r^*\theta_r^* \rangle)$  and iso-contours are used for  $\langle w_r^*\theta_r^* \rangle$ .

The heat transport characteristics at  $x/d=10$  are summarized and a three-dimensional conceptual model is proposed and sketched in Figure 10. The thick and thin red arrows denote the coherent and remainder heat fluxes respectively.

## Conclusions

A 3-D conceptual model is proposed, which is consistent with a previous 2-D model in the plane of mean shear, to account more accurately for the role played by the rib structures in transporting heat and momentum. The transfer of heat out of the vortices appears to be due to the combined effect of coherent and incoherent motions, which occur at different spatial locations. While the coherent heat flux is largely associated with spanwise vortex rolls, the incoherent heat flux occurs between successive opposite-signed vortices, rather than in the saddle region.

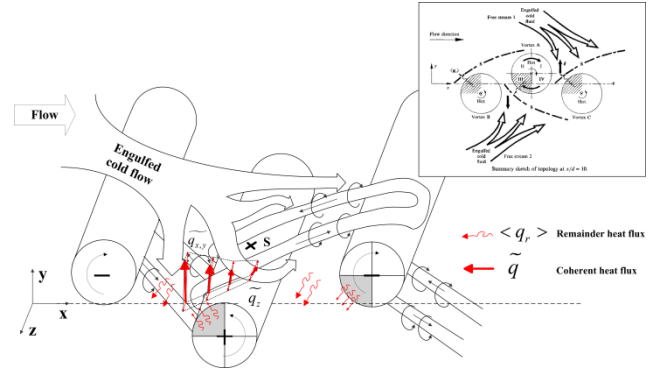


Figure 10. Conceptual model of momentum and heat flux 3D conceptual model of momentum and heat transport at  $x/d=10$ , as compared with the 2D model (inset) of Matsumura & Antonia (1993). The thick and thin red arrows denote the coherent and remainder heat fluxes respectively.

## Acknowledgments

The authors acknowledge the support from the Shenzhen Research Grant (JCYJ20120613134811717). R.A. Antonia acknowledges the support of the ARC.

## References

- [1] Huang, J.F., Zhou, Y. & Zhou, T. Three-dimensional wake structure measurement using a modified PIV technique, *Exp. Fluids*, 40, 2006, 884-896.
- [2] Hussain, A.K.M.F. Coherent structures-reality and myth, *Phys. Fluids*, 26, 1983, 2816-2850.
- [3] Marasli, B., Nguyen, P. & Wallace, J. M. A Calibration Technique for Multi-sensor Hot-Wire Probes and Its Application to Vorticity Measurements in the Wake of a Circular Cylinder, *Exp. Fluids*, 15, 1993, 209-218.
- [4] Matsumura, M. & Antonia, R.A. Momentum and heat transport in the turbulent intermediate wake of a circular cylinder, *J. Fluid Mech.*, 250, 1993, 651-668.
- [5] Mi, J., & Antonia, R.A. Vorticity characteristics of the turbulent intermediate wake, *Exp. Fluids*, 20, 1996, 383-394.
- [6] Scarano, F. & Poelma, C. Three-dimensional vorticity patterns of cylinder wakes, *Exp. Fluids*, 47, 2009, 69-83.
- [7] Wu, J., Sheridan, J., Welsh, M.C. & Hourigan, K. T. Three-dimensional vortex structures in a cylinder wake, *J. Fluid Mech.*, 312, 1996, 201-222.
- [8] Yiu, M.W., Zhou, Y., Zhou T. & Cheng L. Reynolds number effects on three-dimensional vorticity in a turbulent wake, *AIAA Journal*, 42, 2004, 1009-1016.
- [9] Yiu, M.W. Zhou, Y & Zhu Y. Passive scalar transport in a turbulent cylinder wake in the presence of a downstream cylinder, *Flow Turbulence and Combustion*, 72, 2004, 449-461.
- [10] Zhang, H.J., Zhou, Y. & Antonia, R.A. Longitudinal and spanwise vortical structures in a turbulent near wake, *Phys. Fluids*, 12, 2000, 2954-2964.
- [11] Zhou, Y. & Yiu, M.W. Flow structure, momentum and heat transport in a two-tandem-cylinder wake, *J. Fluid Mech.*, 548, 2006, 17-48.
- [12] Zhou, Y., Zhang, H.J. & Yiu, M.W. The turbulent wake of two side-by-side circular cylinders, *J. Fluid Mech.*, 458, 2002, 303-332.
- [13] Zhou, T., Zhou, Y., Yiu, M.W. & Chua, L.P. Three dimensional vorticity in a turbulent cylinder wake, *Exp. Fluids*, 35, 2003, 459-471.